Available online at www.sciencedirect.com
ScienceDirect
International Journal of Multiphase Flow 34 (2008) 76–101
International Journal of Multiphase Flow
www.elsevier.com/locate/ijmulflow

Behaviour of macroscopic rigid spheres in lid-driven cavity flow

S.J. Tsorng [a,b], H. Capart [a,b,*], D.C. Lo [c], J.S. Lai [b], D.L. Young [a,b]

[a] Department of Civil Engineering, National Taiwan University, Taiwan
[b] Hydrotech Research Institute, National Taiwan University, Taiwan
[c] Research Institute of Navigation Science, National Kaohsiung Marine University, Taiwan

Received 30 March 2007; received in revised form 25 June 2007

Abstract

Experiments are conducted to investigate the behaviour of macroscopic rigid particles suspended in a fully three-dimensional viscous flow. The flow considered takes place in a closed cubic cavity, steadily driven along its upper face by a translating lid. Navier–Stokes computations are first performed to characterize the fluid flow, and the resulting kinematic template is checked using laser-illuminated micro-particles. Nearly neutrally buoyant rigid spheres are then inserted in the cavity, and their three-dimensional motions are tracked using stereoscopic imaging. The measured macro-particle motions are compared with those of simulated passive tracers, and their responses to changes in experimental conditions are examined. Although steric effects are observed to hinder passage through narrow throats of the flow field, macro-particle trajectories are otherwise found to align closely with passive tracer paths. The macro-particle orbits, however, are not evenly distributed within the cavity, and cluster closer to the periphery as the Reynolds and Stokes numbers increase. With support from observations of particle rotations relative to the fluid, we interpret this behaviour as resulting from weak forces pulling the macroscopic spheres towards preferential paths, similar to the Segré–Silberberg effect in Poiseuille flow.

Keywords: Cavity flow; Particles; Trajectories

1. Introduction

Isolated rigid bodies of small but finite size suspended in viscous fluids are of interest in many situations. Examples include idealized blood clots in veins and arteries, or macroscopic tracer particles in visualization studies (Swaminathan et al., 2006; Tsorng et al., 2006). In applications, one may be interested in predicting the fate of macro-particles entrained in a given flow, or in interpreting observed particle paths to reconstruct an unknown flow field. In both cases, a key issue concerns the relationship of macro-particle trajectories to fluid paths in the corresponding particle-free flow field. Paraphrasing Aref (1990), to what extent do the

* Corresponding author. Address: Department of Civil Engineering, National Taiwan University, Taiwan. Tel.: +886 2 2923 4703; fax: +886 2 2363 1558.
E-mail address: hcapart@yahoo.com (H. Capart).

0301-9322/$ - see front matter
doi:10.1016/j.ijmultiphaseflow.2007.06.007

trajectories of physical particles match the kinematic template provided by hypothetical point-like tracers passively advected by the flow?

Consider the case of Poiseuille flow, or laminar flow in a long circular tube, in which a neutrally buoyant rigid sphere is inserted. In the Stokes flow limit, symmetry considerations require that the sphere translate along a parallel streamline of the undisturbed flow. Because the equations governing inertialess solid and fluid motions are invariant under time reversal, no normal-to-streamline motions can occur regardless of the radial position of the sphere (Bretherton, 1962; Pozrikidis, 1992). In laminar flow at finite Reynolds number, however, it was shown experimentally by Segré and Silberberg (1961, 1962) that rigid spheres in Poiseuille flow do move across streamlines, migrating towards a preferential annulus of the tube cross-section.

The Segré–Silberberg effect can be attributed to lateral forces between the spheres and the viscous fluid, caused by distortions of the laminar flow by the rigid body. Macroscopic spheres are consequently drawn towards equilibrium radial positions within the tube, where these forces balance out. Much work has been devoted to elucidating the underlying mechanisms. The parameters that intervene include the Reynolds number (Segré and Silberberg, 1962; Asmolov, 1999), particle size (Han et al., 1999), particle rotations (Rubinow and Keller, 1961; Saffman, 1965), the gradient of the shear rate (Feng et al., 1994) and interactions with bounding walls (Ho and Leal, 1974; Eloot et al., 2004). For Poiseuille flow, the interplay of these factors is being increasingly well understood, with recent insights provided by new experiments (Matas et al., 2004a; Staben and Davis, 2005) and direct numerical simulations (Hu, 2001; Inamuro et al., 2000; Hu et al., 2001; Feng and Michaelides, 2003; Pan and Glowinski, 2005; Yang et al., 2005). An informative overview is provided by Matas et al. (2004b).

No equivalent understanding has been attained, however, concerning the behaviour of macroscopic rigid spheres in more general three-dimensional viscous flows. For more general flows, two challenges must be addressed. First, the structure of the flow field in the absence of solid particles must be documented in detail. In contrast with the Poiseuille flow case, this kinematic template will not be known analytically, and must be derived from experiments or numerical solutions of the Navier–Stokes equations. Secondly, one must be able to probe the response of macro-particles suspended in this flow field. In the present work, we address these challenges for the case of neutrally buoyant spheres suspended in a lid-driven cubic cavity. The lid-driven cavity is chosen because it is relatively simple to set up in laboratory experiments and computational simulations, yet generates flows with a rich three-dimensional structure.

In the absence of solid particles, lid-driven cavity flows have been studied extensively. Among others, Chien et al. (1986), Shankar (1998), and Hwu (2006) used analytical approaches to study cavity flows in the inertialess limit. For finite Reynolds numbers, laboratory experiments have been conducted by Pan and Acrivos (1967), Koseff and Street (1984a,b,c), Rhee et al. (1984), Prasad and Koseff (1989), Guermond et al. (2002), Migeon (2002) and Migeon et al. (2003). Numerical investigations include the studies of Burggraf (1966), Freitas et al. (1985), Perng and Street (1989), Zang et al. (1993), Ramanan and Homsy (1994), Chiang et al. (1998), Shu et al. (2003), and Lo et al. (2005). A review summarizing both experimental and numerical work has been given by Shankar and Deshpande (2000).

Two dimensionless numbers can be used to gauge the relative influence of viscosity and inertia on the fluid and particle motions (Batchelor, 1967). The liquid flow pattern inside the lid-driven cavity depends on Reynolds number (Koseff and Street, 1984a; Chiang et al., 1998; Shankar and Deshpande, 2000)

$$Re = \frac{US}{\nu}, \tag{1}$$

where U is the lid speed, S the side length of the cubic cavity, and ν the kinematic viscosity of the liquid. The motions of macroscopic solid particles suspended in the flow, on the other hand, can be characterized by Stokes number

$$St = \frac{\tau_M}{\tau_f} = \frac{\rho_M d_M^2 U}{18\rho_f \nu S} = \frac{1}{18}\frac{\rho_M}{\rho_f}\frac{d_M^2}{S^2}Re, \tag{2}$$

where $\tau_M = \frac{1}{18}\rho_M d_M^2/(\rho_f \nu)$ represents the response time of a macro-particle of diameter d_M and density ρ_M in a fluid of density ρ_f and kinematic viscosity ν (Prevost et al., 1996; Yang and Shy, 2005; Chen et al., 2006), and where $\tau_f = S/U$ is a characteristic time scale of the lid-driven fluid motion inside the cavity. A small Stokes

number indicates that viscous drag has ample time to attenuate any velocity discrepancy between the particle and its surrounding fluid. A large Stokes number, by contrast, suggests weaker viscous coupling allowing the particle to deviate from the fluid motions. In the present study, we consider cavity Reynolds numbers in the range $Re = 130$ to 3200, corresponding to Stokes numbers in the range $St = 0.006$ to 0.161.

To examine the behaviour of macroscopic particles in lid-driven cavity flows, the present paper relies on a combination of computations and experiments. The corresponding methods are summarized in Section 2, and have been documented earlier by Lo et al. (2005) and Tsorng et al. (2006). In Section 3, the three-dimensional fluid flow field at $Re = 470$ is characterized in detail. The resulting kinematic template is also checked against laboratory observations of laser-illuminated micro-particles. Measurements of macro-particle motions at the same Reynolds number are then presented in Section 4. The three-dimensional trajectories of rigid spherical particles are tracked using stereoscopic imaging, and compared with the simulated paths of passive tracers. In Section 5, the empirical behaviour of macro-particles is probed further by examining particle responses to changes in experimental conditions. Change from slightly negative to slightly positive buoyancy is considered, as well as variations of the cavity Reynolds number. Section 6, finally, summarizes our observations and interpretations.

2. Apparatus and methods

2.1. Experimental set-up and imaging measurements

Experiments are conducted using the device illustrated on Fig. 1a. The flow of interest takes place in a cubic cavity of side $S = 10$ cm, with bottom, side and end walls made of acrylic panels. The top face is a moving lid consisting of a motor-driven conveyor belt, operated at speeds in the range $U = 3.5$–32 cm/s. The conveyor belt rig is supported laterally and placed upside down, with the lower face of the belt grazing the top edges of the cavity walls. An outer tank surrounds the lid-driven cavity, and the test liquid fills both the inner and outer enclosures, half submerging the conveyor belt. This ensures that the inner cavity remains filled with liquid. To guarantee optical access, both enclosures have transparent sides. More construction details and photographs of the set-up are provided in Tsorng (2006). A lid-driven cavity of similar design was used earlier by Koseff and Street (1984a).

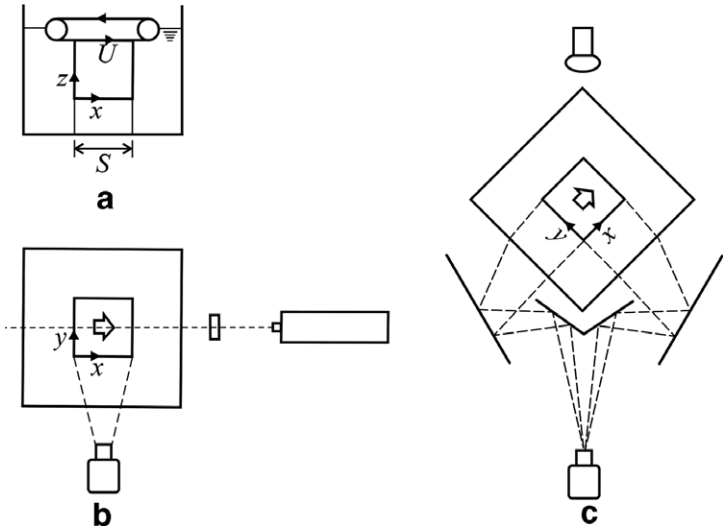

Fig. 1. Experimental set-up: (a) side view of the cavity, lid drive mechanism, and outer enclosure; (b) top view of the laser sheet and camera configuration used to record micro-particle tracks; (c) top view of the camera and mirror configuration used for stereo measurements of macro-particle trajectories.

Imaging methods are used to capture the motions of particles suspended in the lid-driven liquid flow. Two types of particles are examined. First, microscopic particles made visible by laser sheet illumination are used to visualize the flow in selected planes. Secondly, spherical plastic beads are selected to examine the behaviour of macroscopic rigid particles inserted in the flow. The liquid chosen is a high-viscosity mixture of water and glycerol. Its composition can be adjusted to closely match the density of the macroscopic beads. For a given composition, the kinematic viscosity of the mixture v is measured, and the speed U of the conveyor belt is set to obtain the desired value of the cavity Reynolds number $Re = US/v$.

The micro-particles used for flow visualization are hollow glass spheres supplied by the company TSI. These particles have a mean diameter $d_\mu = 10$ μm and a density $\rho_\mu = 1500$ kg/m^3. Using Stokes' law, the corresponding fall speed in the water–glycerol mixture is less than 5 μm/s. This is negligible compared to the typical flow velocities in the cavity. For particles of this size (above the colloidal range), Brownian diffusion can also be disregarded. The micro-particles are introduced into the flow in two different ways. They can be mixed with the liquid inside the cavity before an experiment begins. Or, they can be mixed with liquid injected into the cavity during an experiment. The particles are invisible under ambient light but shine brightly under laser illumination. The laser used for that purpose is a 300 mW ion laser emitting a light beam of wavelength equal to 488 nm. A semi-cylindrical lens is used to transform the beam into a light sheet having a divergence angle of 20°.

The imaging configuration adopted to observe the micro-particle motions is illustrated on Fig. 1b. The laser light sheet is oriented parallel to the x–z plane at the desired lateral position y, and the flow is imaged from the side using digital video. The video sensor used is an AVT camera connected to a computer using the IEEE 1394 port and piloted using the open source software Coriander. The CCD camera has a resolution of 1024 by 768 pixels and operates at a frequency of 15 frames per second. To visualize particle tracks, the digital frames are used to construct artificial long exposure images. These are obtained from a sequence of frames by retaining the brightest value experienced at each pixel position.

The second set of experiments is conducted with macro-particles instead of micro-particles. The macroscopic particles used are spherical plastic beads of diameter $d_M = 3$ mm and density $\rho_M = 1210$ kg/m^3. To approximate neutral buoyancy as closely as possible, the composition of the water–glycerol mixture is adjusted until solid particles are suspended in the liquid with minimal vertical drift. This is difficult to achieve for large particles (Staben and Davis, 2005). Regardless of the care taken, therefore, a small density mismatch will remain, and may have an effect on the particle behaviour in the cavity flow. To control for this effect, we will describe experiments with both positive and negative buoyancy.

For the positive buoyancy experiments, the liquid composition is adjusted to be slightly heavier than the particles, causing them to rise slowly in liquid at rest at a speed of 4 mm/min. At this composition, the measured kinematic viscosity of the liquid is $v = 37.2$ mm^2/s. Applying Stokes' law, the corresponding relative density mismatch $(\rho_f - \rho_M)/\rho_f$ is approximately 0.05%. For the negative buoyancy experiments, on the other hand, the liquid composition is tuned to be slightly lighter than the particle, yielding slow fall speeds of 13 mm/min. The corresponding kinematic viscosity is $v = 17.3$ mm^2/s, and the relative density mismatch is approximately −0.07%. The liquid temperatures before and after an experiment were checked to differ by no more than 0.1 °C.

The macroscopic rigid spheres are opaque and easy to identify on back-illuminated views of the cavity. Their motions can therefore be tracked throughout the flow volume using stereoscopic imaging. The imaging configuration adopted is illustrated on Fig. 1c. A single video camera combined with a system of mirrors is used to record particle motions under two mutually orthogonal viewpoints. A view through the back wall of the cavity is recorded on the left half of the video frames, and a side view is recorded on the right half. The camera used is a TRV950 Sony DV camera having a sensor resolution of 480 by 640 pixels. Operating at a frequency of 30 frames per second, the camera can tape footage segments of up to 20 min.

Three-dimensional tracking of the macro-particle motions is performed using the imaging algorithms detailed in Spinewine et al. (2003) and Tsorng et al. (2006). Camera viewpoints are first calibrated using the known positions of the eight corners of the cavity, supplemented by internal points marked on a diagonal calibration target. Two-dimensional particle positions are identified with the illumination maxima of negative images, and refined to sub-pixel accuracy using the methods described in Capart et al. (2002). Using the

calibrated camera viewpoints, stereoscopic rays are traced back into the viewing volume, yielding three-dimensional particle positions at intersections between rays.

Measurements extracted from a sequence of stereo frames can then be assembled into time series of particle positions. To reduce measurement noise, raw position histories are finally processed using a Kalman filter (Kalman, 1960), applied to the data along both forward and backward passes to avoid phase errors. Details of the methods used are presented in Tsorng et al. (2006), while an error analysis was conducted by Tsorng (2006). Estimated root-mean-square errors on the raw particle positions are approximately 0.4 mm, and are reduced to approx. 0.2 mm after Kalman filtering.

2.2. Navier–Stokes computations

To complement the experiments, numerical computations of the three-dimensional flow inside the cavity are performed. The incompressible viscous flow is solved in the absence of solid particles, using the velocity–vorticity form of the Navier–Stokes equations. The equation governing the evolution of the vorticity vector $\boldsymbol{\omega}$ is (see e.g. Batchelor, 1967)

$$\frac{\partial \boldsymbol{\omega}}{\partial t} = -\mathbf{u}\cdot\nabla\boldsymbol{\omega} + \boldsymbol{\omega}\cdot\nabla\mathbf{u} + \nu\nabla^2\boldsymbol{\omega} = \mathbf{f}, \tag{3}$$

where velocity vector $\mathbf{u}$ has Cartesian components (u,v,w), vorticity vector $\boldsymbol{\omega} = \nabla\times\mathbf{u}$ has components (ξ,η,ζ), $\nabla = (\partial/\partial x,\ \partial/\partial y,\ \partial/\partial z)$ is the 3D gradient operator, and ν is the kinematic viscosity of the liquid. Vector $\mathbf{f} = (f,g,h)$ sums the contributions to the rate of change of vorticity due to convective transport, vortex stretching and tilting, and viscous diffusion. Since our interest lies in the steady flow pattern inside the cavity, Eq. (3) is integrated in time until convergence to steady flow is achieved. The scheme used for this purpose is a modified version of the scheme described in Lo et al. (2005). Time-stepping is performed using the following third-order Total Variation Diminishing (TVD) Runge–Kutta method (Shu and Osher, 1988):

$$\boldsymbol{\omega}' = \boldsymbol{\omega}(t) + \Delta t\mathbf{f}(\boldsymbol{\omega}(t),\mathbf{u}(t)), \tag{4a}$$

$$\boldsymbol{\omega}'' = \frac{3}{4}\boldsymbol{\omega}(t) + \frac{1}{4}\boldsymbol{\omega}' + \frac{1}{4}\Delta t\mathbf{f}(\boldsymbol{\omega}',\mathbf{u}'), \tag{4b}$$

$$\boldsymbol{\omega}(t+\Delta t) = \frac{1}{3}\boldsymbol{\omega}(t) + \frac{2}{3}\boldsymbol{\omega}'' + \frac{2}{3}\Delta t\mathbf{f}(\boldsymbol{\omega}'',\mathbf{u}''). \tag{4c}$$

For the spatial operators, finite differences are used on a Marker And Cell (MAC) staggered grid. The first component of vector $\mathbf{f}$, for instance is computed using statement

$$f(\boldsymbol{\omega},\mathbf{u}) = -\frac{\delta_y(v\xi)}{\Delta y} - \frac{\delta_z(w\xi)}{\Delta z} + \frac{\delta_y(\eta u)}{\Delta y} + \frac{\delta_z(\zeta u)}{\Delta z} + \nu\left(\frac{\delta_x^2}{(\Delta x)^2} + \frac{\delta_y^2}{(\Delta y)^2} + \frac{\delta_z^2}{(\Delta z)^2}\right)\xi, \tag{5}$$

where δ_α and δ_α^2 are the first- and second-order central difference operators in direction $\alpha = x$, y, or z. At each step, the velocity field $\mathbf{u}$ must be retrieved from the vorticity field $\boldsymbol{\omega}$. This can be done by solving the Poisson equation

$$\nabla^2\mathbf{u} = -\nabla\times\boldsymbol{\omega}, \tag{6}$$

using the well-documented iterative method of Gary et al. (1983). In the present work, only the velocity components u and v are obtained in this fashion. For the third velocity component w, we use instead the differentiated form of the continuity equation

$$\frac{\partial^2 w}{\partial z^2} = -\frac{\partial}{\partial z}\left(\frac{\partial u}{\partial x} + \frac{\partial v}{\partial y}\right), \tag{7}$$

integrated with the help of a tri-diagonal matrix solver. Proposed by Wu et al. (1995), this approach provides an efficient and accurate way of retrieving the third velocity component. For the lid-driven cavity flow, no flux and no slip boundary conditions are applied along the five static faces and along the moving top lid where velocity component u is set equal to the belt speed U.

To validate the code, computations are first performed for $Re = 400$. For this particular Reynolds number, calculations of the lid-driven cubic cavity flow have been obtained earlier by Shu et al. (2003) and Lo et al. (2005) using differential quadrature and finite differences, respectively. Their benchmark results for the velocity profiles along longitudinal and vertical centrelines are plotted on Fig. 2a, and compared with our calculations for uniform meshes of 20^3, 40^3, 60^3 and 80^3 cells. Convergence is verified, and our results for $80 \times 80 \times 80$ cells are in good agreement with the benchmark data. This discretization will be used for all the calculations discussed below. In Fig. 2b, our converged computations are compared with the PIV measurements of Tsorng (2006), obtained in the lid-driven cavity described in the previous sub-section. Reasonable agreement is obtained, providing some further confidence in the approach.

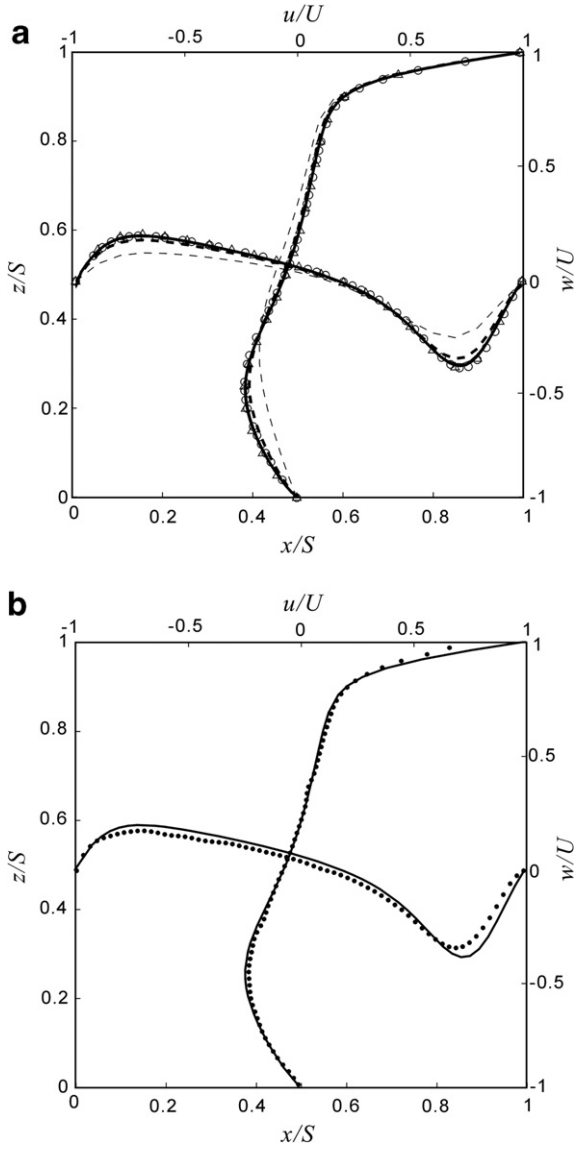

Fig. 2. Velocity profiles along the longitudinal and vertical centrelines of the cubic cavity at $Re = 400$: (a) computed results for 20^3 (thin dashes), 40^3 (thick dashes) 60^3 cells (thin solid lines) and 80^3 cells (thick solid lines) compared to the calculations of Shu et al. (2003, triangles) and Lo et al. (2005, circles); (b) Computations for 80^3 cells (solid lines) compared with the PIV measurements (dots) of Tsorng (2006).

3. Flow structure at $Re = 470$

Before examining the response of suspended macro-particles, the structure of the flow field must be characterized in detail. We consider here the case of $Re = 470$, for which our results are most complete. In the absence of macro-particles, we adopt three different means to characterize the flow field. In a first sub-section, results from Navier–Stokes computations of the pure fluid flow field are used to visualize the three-dimensional flow structure. In a second sub-section, the calculated streamlines in selected planes are compared with experimental micro-particle tracks, and used to delineate different eddy regions of the flow. Thirdly, the existence of pathways connecting primary and corner eddies is checked by comparing the dispersal patterns of simulated tracers with those of injected micro-particles.

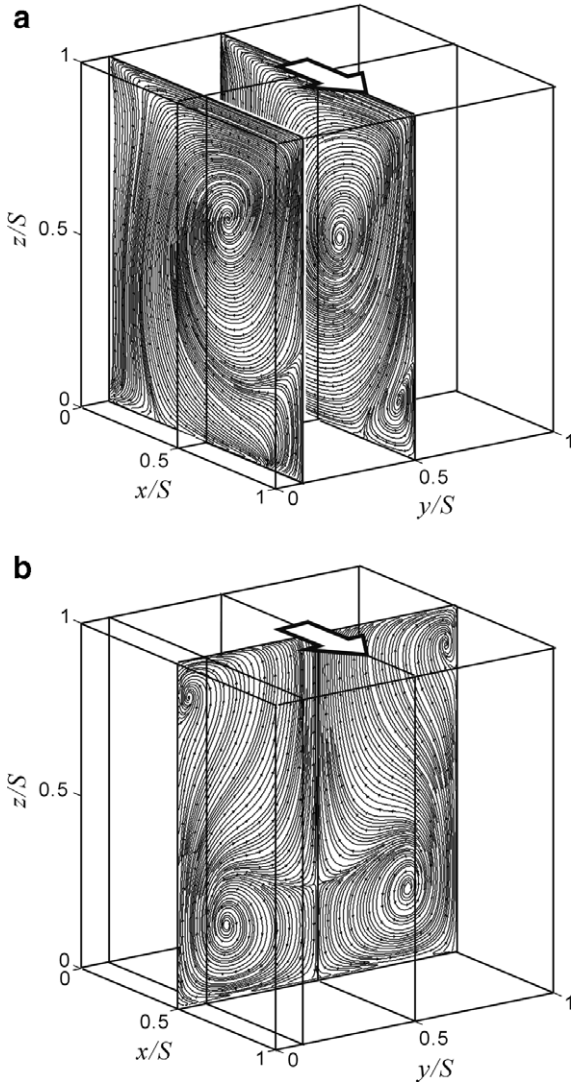

Fig. 3. Three-dimensional structure of the lid-driven cavity flow at $Re = 470$: (a) computed streamlines in longitudinal planes $y/S = 0.1$ and $y/S = 0.5$; (b) computed streamlines in the central transverse plane $x/S = 0.5$.

3.1. Three-dimensional flow structure

Computed results for the pure fluid flow can first be used to visualize the three-dimensional flow structure at $Re = 470$. Fig. 3 shows calculated streamlines in selected longitudinal and transverse planes. As illustrated in panel 3a, the x–z flow pattern is dominated by a large primary eddy, driven by the moving top lid and occupying most of the cavity. Since the flow is three-dimensional, the vortex streamlines do not form closed loops. Instead, they spiral inward and outward. Near the sidewall ($y/S = 0.(1)$, an inward spiral is associated with suction of the fluid particles towards the core of the primary eddy. Along the longitudinal centre plane ($y/S = 0.5$), by contrast, fluid particles spiral outwards, away from the primary vortex core and towards the perimeter of the cavity. It can be noted that the centre of the primary eddy is located away from the cavity centre. Longitudinally, the vortex centre is displaced towards the downstream end wall. Vertically, it is displaced towards the top lid, the more so for slices closer to the sidewall. In the medial plane $y/S = 0.5$, a conspicuous secondary eddy is observed in the lower downstream corner of the cavity.

The three-dimensional flow structure is further illustrated in panel 3b. Here the lateral and vertical fluid motions are depicted in the central transverse plane ($x/S = 0.5$). The streamlines in the $y-z$ plane show clearly the pattern of sideways circulation. Fluid particles are drawn towards the longitudinal centre plane ($y/S = 0.5$) over most of the cavity interior, and the return flow towards the sidewalls is relegated to the periphery. At this Reynolds number, the flow field is steady and laterally symmetric. Pairs of spiral nodes are observed on both sides of the cavity: outward spiral nodes near the bottom, and inward spiral nodes near the top close to the sidewalls. These are respectively associated with Taylor–Görtler-like vortices and with end-wall vortices (Koseff and Street, 1984a; see also Chiang et al., 1997; Shankar and Deshpande, 2000). A saddle point is located near the lower third of the vertical centre line. More detailed sets of cross-sections will be presented below and compared with experimental results for both micro- and macro-particle motions.

3.2. Comparison of calculated fluid streamlines with observed micro-particle tracks

To check the above picture, calculated results can be compared with micro-particle motions in selected two-dimensional slices of the flow field. Fig. 4 compares laser-illuminated micro-particle tracks against calculated streamlines in x–z planes having lateral intercepts $y/S = 0.1$, 0.2, 0.3 and 0.4. For the experiments depicted on the left panels of this figure, the micro-particles were first thoroughly mixed with the liquid inside the cavity. The conveyor belt was then placed atop the cavity, and operated at constant speed for 10 min before performing any image acquisition. For each intercept y/S, an image sequence was acquired after adjusting the position of the laser light sheet. The artificial long exposure images were later constructed from video sequences of 900 successive images, amounting to a time span of 60 s.

The right panels of Fig. 4 show calculated streamlines at the same Reynolds number $Re = 470$, and at the same y/S intercepts. They are extracted from the full volume numerical results used earlier to construct Fig. 3. Comparison of the left and right panels of Fig. 4 indicates close agreement between the observed and calculated flows. The streamline patterns are in good agreement, both for the inward spirals of the near wall region and for the outward spirals near the cavity centre plane. Overall, the Navier–Stokes calculations accurately predict the flow field. The comparison also suggests that the micro-particle tracks closely approximate the fluid streamlines, as would be expected for passively advected particles in a steady flow field.

The streamline patterns shown on Fig. 4 can also be used to delineate different flow regions. In the present context, we are particularly interested in distinguishing the primary vortex region from the rest of the flow. For this purpose, we define on each slice a demarcation line tracing the outer boundary of the primary eddy. Following Chiang and Sheu (1997), this demarcation line is chosen as the flow streamline that is connected to a detachment or reattachment point along the cavity perimeter. On panels 4e and f, the line is traced forward from its detachment point on the downstream end wall. On panels 4g and h, on the other hand, the line is traced backward from its reattachment point on the upstream end wall. Away from their detachment or reattachment points, the lines do not have any clear termination point. There is no slice in which one can completely enclose the primary eddy within a single streamline. Nevertheless, each demarcation line provides a reasonably objective boundary, separating the inner primary eddy from a lower and outer region that includes the downstream secondary eddy.

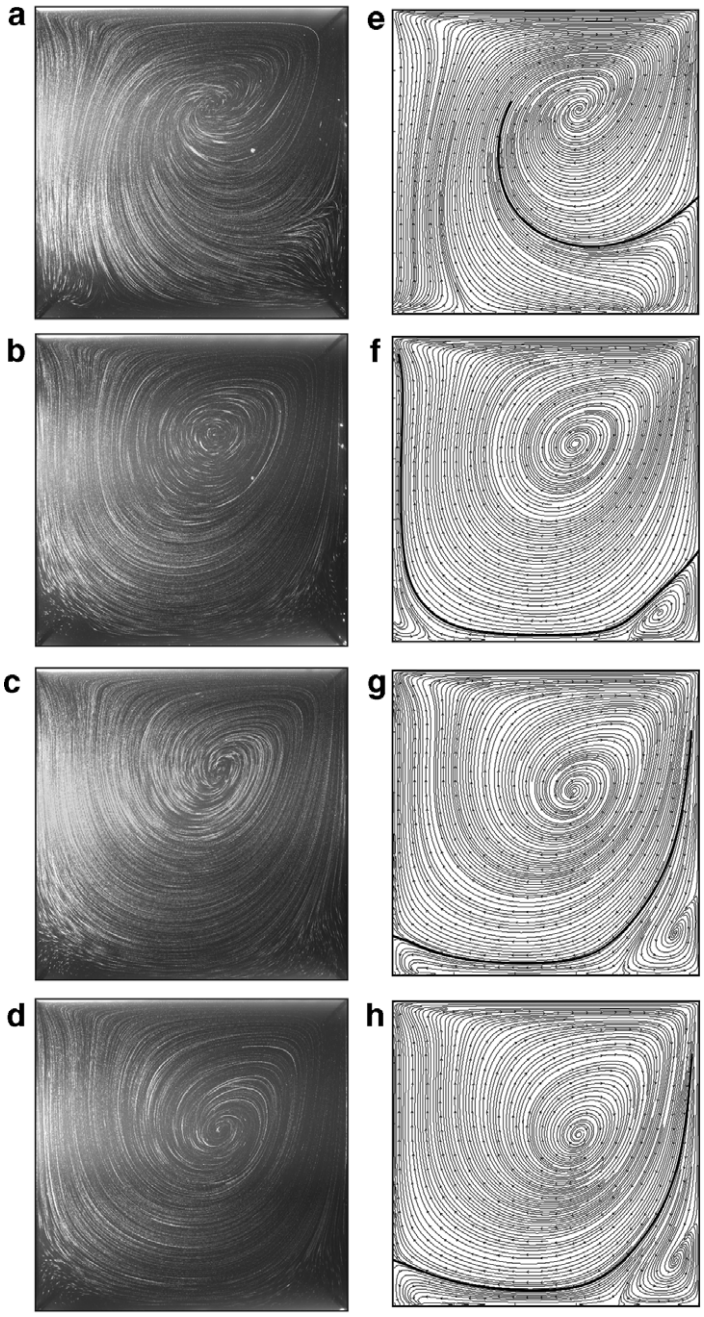

Fig. 4. Comparison of laser-illuminated micro-particle tracks (left panels), with calculated streamlines (right panels) in selected longitudinal planes: (a,e) $y/S = 0.1$; (b,f) $y/S = 0.2$; (c,g) $y/S = 0.3$; (d,h) $y/S = 0.4$.

The family of demarcation lines extracted in this way from a more complete set of longitudinal slices is shown in three-dimensional view in Fig. 5. The resulting envelope defines a partial bounding surface between the primary eddy on the inside and the corner and bottom wall region on the outside. We emphasize again that this boundary is not a closed surface wrapped around the primary vortex. Also, the surface is only partially attached to the solid boundaries. The surface is open at the top of the downstream end wall near the centre plane of the cavity, and open in the upper upstream corner near the cavity side wall. Due to lateral symmetry,

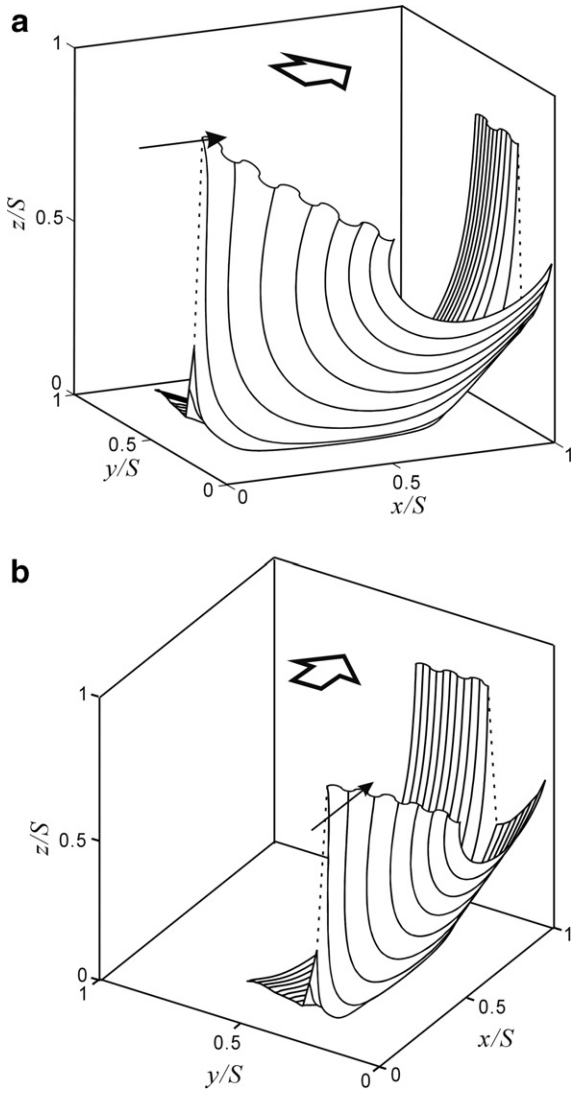

Fig. 5. Three-dimensional views of the demarcation lines defined in Fig. 4. Their envelope defines a partial bounding surface with the primary eddy on the inside and the corner and bottom wall region on the outside. Wavy lines indicate open borders (not attached to a wall), and the thin arrow on panel (b) denotes the injection point used for the micro-particle dispersal tests of Fig. 6.

the cavity is split into separate left and right sides. On each side, however, the different flow regions are connected to each other. This will be further illustrated in the next section.

3.3. Dispersal of injected micro-particles

To gain another perspective on the circulation inside the cavity, a second set of micro-particle experiments was conducted at the same Reynolds number $Re = 470$. For these experiments, the liquid inside the cavity is initially devoid of micro-particles, and the flow is driven at the desired lid speed. Once steady flow has been reached, particle-laden liquid is injected at a single location within the cavity. This is done using a pre-positioned needle having its mouth at coordinates $(x, y, z)/S = (0, 0.025, 0)$. The needle is oriented parallel to the x-direction to match the local direction of the lid-driven flow. Once started, the injection proceeds continuously, at a constant flow rate tuned to match the local flow speed at the point of injection. This adjustment

was done in advance to minimize wake or jet instabilities associated with velocity differences between the flow and the injected stream.

In order to document the ensuing fate of the particle-laden stream, the longitudinal plane $y/S = 0.4$ is illuminated with the laser light sheet and observed from the side using the video camera. Located near the cavity centre plane, this observation slice was chosen because it features at its upper downstream corner an open pathway linking the primary eddy to the downstream secondary eddy. Its location coincides with the laser-illuminated slice shown earlier in Fig. 4h. The injection point, on the other hand, is located in plane $y/S = 0.025$, close to the cavity sidewall. Its precise location, near the top lid, is illustrated in Fig. 5. Because the point of injection lies in another plane, some time will elapse before the injected stream reaches the illuminated slice.

The observed dispersal pattern is depicted on Fig. 6. As seen on panel 6a, the laser-illuminated slice is initially free of particles. Panels Fig. 6b–d show accumulated long exposure images of the ensuing evolution in the laser-illuminated plane. The images were obtained from the raw video footage by registering brightness maxima at each pixel over durations of 60, 120, and 180 s, respectively, starting from the beginning of injection. The observed gradual invasion is consistent with the three-dimensional flow structure discussed earlier. Starting from the injection point near the cavity sidewall, the micro-particles are drawn inwards into the primary vortex. They become visible in the illuminated plane along multiple segments of the spiral pattern. Close to the centre plane, particles spiral outwards and reach the upper downstream corner of the cavity. From there, they proceed through a narrow corridor down the end wall until reaching the secondary eddy in the lower downstream corner. As anticipated, the long winding paths of the micro-particles allow them to move in and out of the primary vortex region.

For comparison, panels e–h of Fig. 6 show simulation results. These are obtained by seeding region $0 < x/S < 1$, $y/S = 0.025$, $0.6 < z/S < 1$ of the domain with tracer particles, then integrating their Lagrangian trajectories. At each step of the integration, velocities are determined from the grid values of the computed steady flow using bilinear interpolation. On the right panels, white and gray tones are used to distinguish the inner and outer regions on both sides of the separation line defined earlier in Fig. 4h. On this background, simulated trajectory segments are recorded when they penetrate slice $0.35 < y/S < 0.45$ associated with the laser-illuminated plane. Panels (f)–(h) of Fig. 6 show the resulting segments accumulated over 60, 120 and 180 s of integration. Although the simulations (right panels of Fig. 6) lag behind the observations (left panels of Fig. 6), they both depict a similar evolution. Like the micro-particles, the passive tracers first enter the primary eddy, then invade the secondary eddy and bottom wall region on the other side of the separation line.

4. Macro-particle motions at $Re = 470$

Experiments conducted with macroscopic rigid spheres can now be examined, and interpreted in light of the kinematic template described in the previous section. Recall that the diameter of the macroscopic spherical beads is $d_M = 3$ mm, to be compared with the side length $S = 10$ cm of the cubic cavity. In this section, we continue to restrict our attention to flows at Reynolds number $Re = 470$, and focus on the behaviour of slightly buoyant beads, having relative density $(\rho_f - \rho_M)/\rho_f \approx 0.05\%$. The corresponding Stokes number is $St = 0.023$. Other Reynolds and Stokes numbers and the case of negatively buoyant macro-particles will be examined in the next section.

4.1. Macro-particle tracks

Using stereoscopic imaging, the path of a single macro-particle can be followed as it moves about the three-dimensional flow. In the experiment we consider, the flow starts from rest, with a slightly buoyant macro-particle placed at the top of the cavity, touching the conveyor belt. At time $t = 0$, the lid motion starts at the prescribed velocity, and the ensuing particle motion is tracked over a duration of 7 min. This includes an initial transient phase estimated to last about 1 min, before the liquid flow settles to a steady state.

Track segments extracted from the measured trajectory of a macro-particle can first be compared against calculated fluid streamlines in selected planes. This is shown in Fig. 7. Panels 7a–d show longitudinal planes at intercepts $y/S = 0.1$, 0.2, 0.3 and 0.4, evenly spaced between the cavity sidewall and the centre plane. The fluid streamlines are obtained from the Navier–Stokes calculations and were presented earlier in Fig. 4.

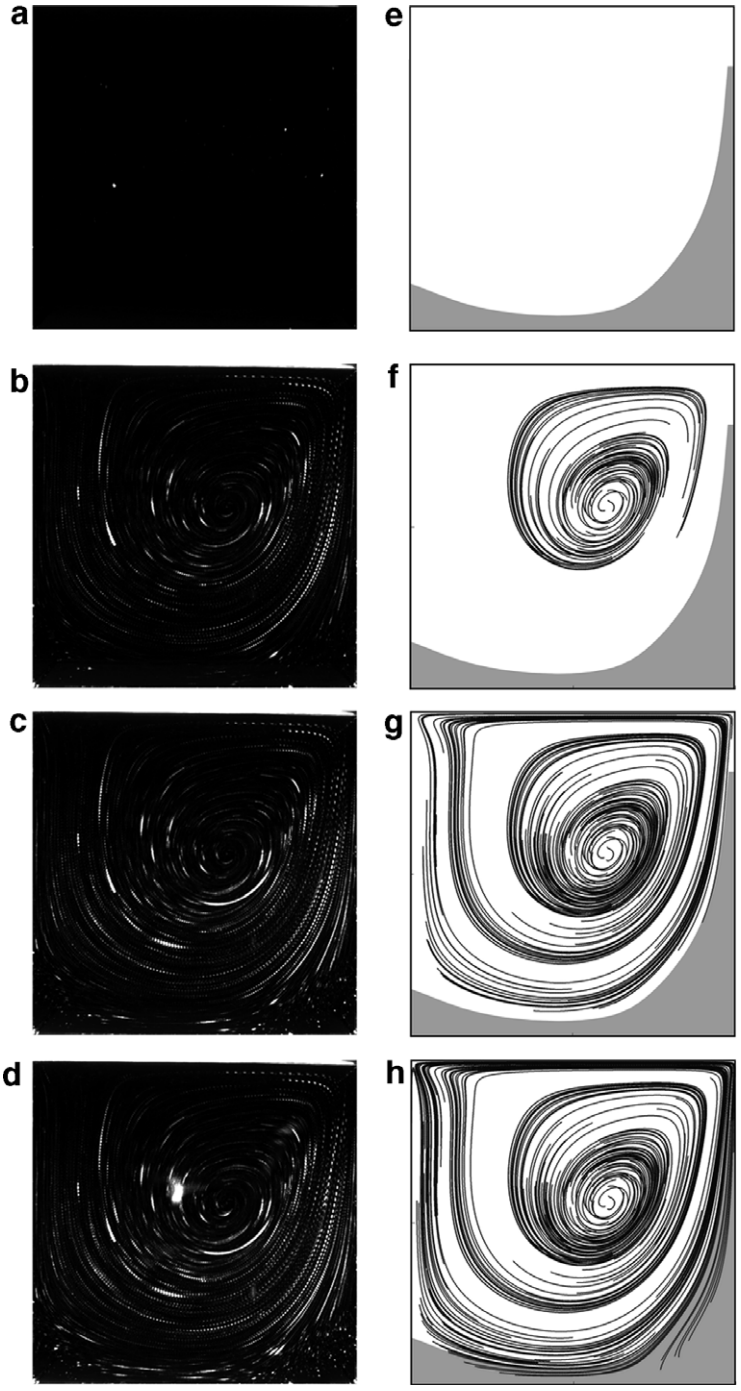

Fig. 6. Dispersal of a stream of particle-laden liquid injected near the sidewall and observed in a thin slice near the cavity centre plane ($y/S = 0.4$): (a–d) accumulated long exposure images of the laser-illuminated plane at times $t = 0$, 60, 120 and 180 s after start of injection (experiment); (e–h) accumulated segments of passive tracer trajectories at times $t = 0$, 60, 120 and 180 s (simulation).

The macro-particle tracks, on the other hand, are trajectory segments recorded when they cross a slice of half width $b = 1.25$ mm on either side of the longitudinal plane considered. Long segments are obtained when the macro-particle motion is tangent to the plane, and conversely short segments result when the particle motion has a significant normal component (for instance near the core of the primary eddy).

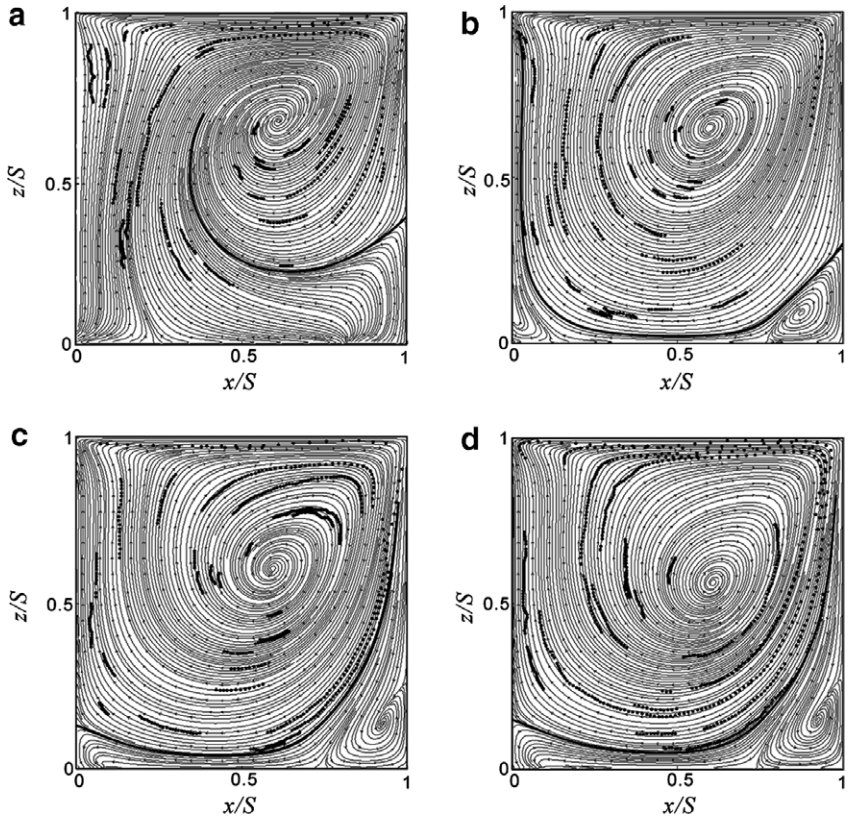

Fig. 7. Comparison of observed macro-particle tracks and calculated fluid streamlines in selected longitudinal planes: (a) $y/S = 0.1$; (b) $y/S = 0.2$; (c) $y/S = 0.3$; (d) $y/S = 0.4$.

Locally, the macro-particle tracks align closely with the fluid streamlines. This suggests that, like the micro-particles examined previously, the macro-particle trajectories coincide with the paths of passive tracers advected by the steady flow. Such alignment is not unexpected given the low value of the Stokes number, implying a strong viscous coupling between particle and fluid. Unlike injected micro-particles and calculated passive tracers, however, the macro-particles do not invade the secondary eddy in the lower downstream corner of the cavity. On panels 7b and c, the macro-particles stay on the inside of the demarcation line. On panel 7d, macro-particle tracks are seen to graze the boundary, but ultimately they do not enter the secondary eddy. Whereas this region was accessible to the micro-particles and passive tracers of Fig. 6, it appears to be avoided by the macro-particles of Fig. 7d.

4.2. Three-dimensional position histories and trajectories

Position histories provide another view of the same experiment. Because stereoscopic measurements are able to follow a macroscopic particle throughout the cavity, a complete history of the particle motions can be assembled. Shown in Fig. 8a–c, time series of the three position components exhibit a sequence of repeating cycles. Although these cycles are somewhat irregular, certain clear patterns emerge. Rapid, out of phase oscillations of the x- and z-components in panels (a) and (c) are associated with loops around the cavity. The amplitude of these loops is modulated by slower sideways motions of the particle in the y-direction (panel b). A typical orbital cycle features three distinct stages: (1) a rapid inward spiral as the particle moves from the near-wall region (right sidewall at $y/S = 0$) towards the centre plane ($y/S = 0.5$); (2) a slow outward spiral during which the particle stays near the centre plane; (3) a rapid excursion back to the near-wall region once the particle has reached the perimeter of the cavity. Although this same pattern keeps on being repeated, the

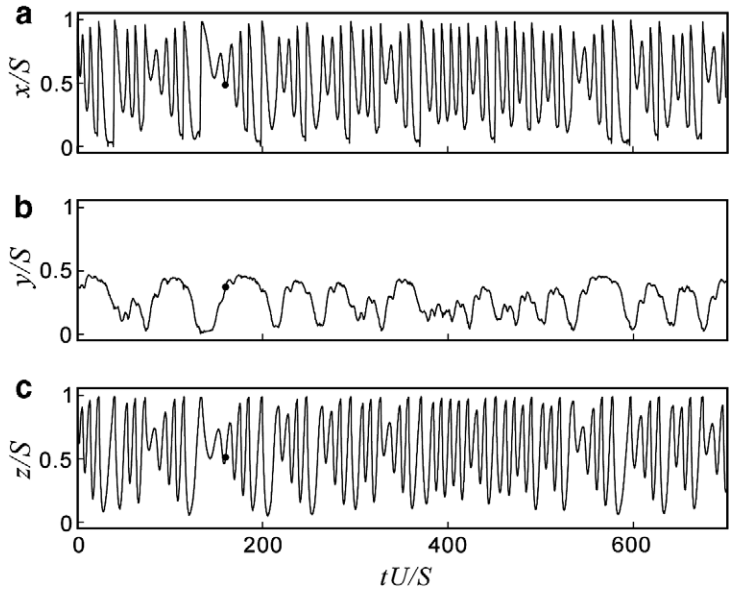

Fig. 8. Extended time series of the measured 3D position of a slightly buoyant macro-particle suspended in the lid-driven cavity flow at $Re = 470$ ($St = 0.023$).

length of each cycle varies, without any clear periodicity. As seen on Fig. 8b, short cycles alternate with long cycles of up to 6 loops around the cavity as the particle makes its way from the wall to the centre and back again.

The measured macro-particle position history can be compared with simulation results for a passive tracer advected by the flow at the same Reynolds number. For this purpose, a simulated path is integrated numerically through the steady flow field derived from the Navier–Stokes computations. At each time step of the integration, the particle velocity is assumed to coincide with the local fluid velocity interpolated from the calculated flow field. To facilitate comparison with the observed results, the starting point of the integration is chosen as the measured position of the macro-particle at dimensionless time $tU/S = 160$. This time is chosen instead of time $t = 0$ to avoid the start-up transient. To obtain nonetheless a complete time history, the simulated path is integrated both forward and back. The results are shown in Fig. 9.

Because errors accumulate over the integration, one would not expect the observed and simulated time histories to agree with each other for long, even if the macro-particle behaved exactly like a passive tracer. Except for a short interval of time around the starting point of the integration, therefore, the time histories can only be compared in their general features. From this point of view, the observed and simulated histories of Figs. 8 and 9 are quite similar in character. Like the observed macro-particle, the simulated passive tracer undergoes rapid loops in the x–z plane, with amplitudes that are modulated by irregular cycles between the centre plane and the side wall in the spanwise y-direction. There is however one segment of the passive tracer position history that is qualitatively different from the cycles observed in the macro-particle experiment. Between dimensionless times $tU/S = 200$ and 250, the passive tracer temporarily interrupts its looping motion to linger along the downstream end wall of the cavity.

To clarify the corresponding contrast in behaviour, Fig. 10 shows a close-up comparison of the measured and simulated position histories over time interval $100 < tU/S < 350$. Three-dimensional views of the associated particle trajectories are presented in Fig. 11. Over sub-interval $150 < tU/S < 200$, the observed and simulated time histories are in rather close agreement. Going forward in time, both the macro-particle and passive tracer undergo first a sequence of three loops, gradually spiraling outwards near the centreplane of the cavity. Around time $tU/S = 200$, however, the two paths diverge. Shown in Fig. 11a, the macroscopic particle continues to loop around the primary eddy. Meanwhile, as seen in Fig. 11b, the simulated passive tracer makes a conspicuous excursion to the downstream corner region. The tracer passes from primary to corner eddy along

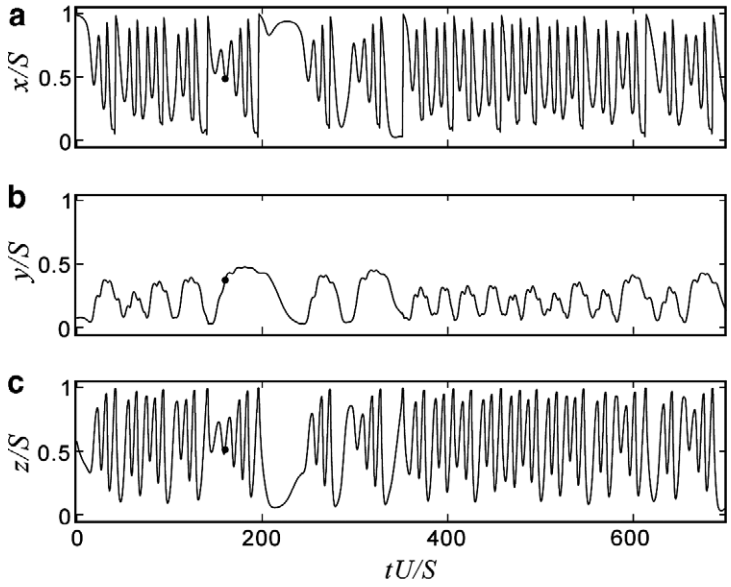

Fig. 9. Extended time series of the simulated 3D position of a passive tracer advected by the pure fluid flow field at $Re = 470$.

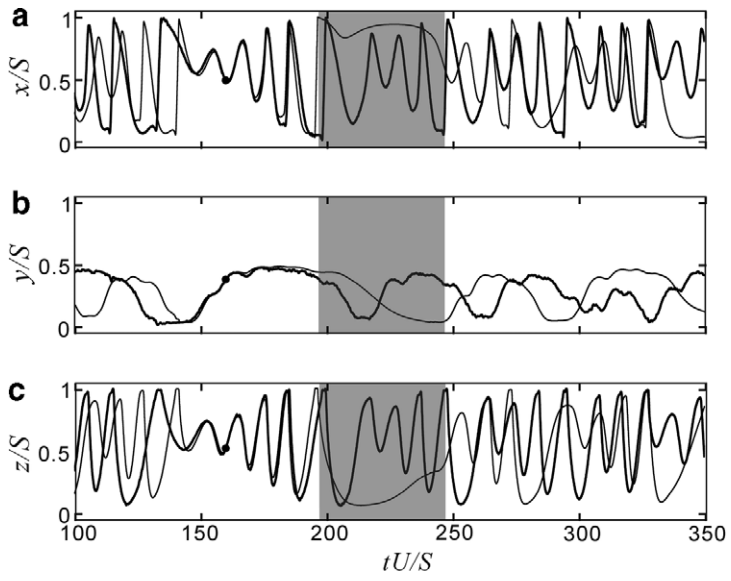

Fig. 10. Close-up comparison of the position histories of an observed macro-particle (thick lines) and simulated passive tracer (thin line), both starting from the same point (black dot). The segment during which the passive tracer (but not the macro-particle) makes an excursion into the corner eddy is highlighted in gray.

the downstream end wall, slowly drifts towards the sidewall, then turns back to re-enter the primary eddy. In all the experiments that we have conducted (some 15 runs), macroscopic particles were never observed to make such excursions to the downstream corner eddy.

4.3. Narrow pathways and steric effects

As indicated earlier by the results of Fig. 6, a passive tracer can thus move freely between the primary and corner eddy regions, whereas a macro-particle does not. The observed difference in behaviour can most simply

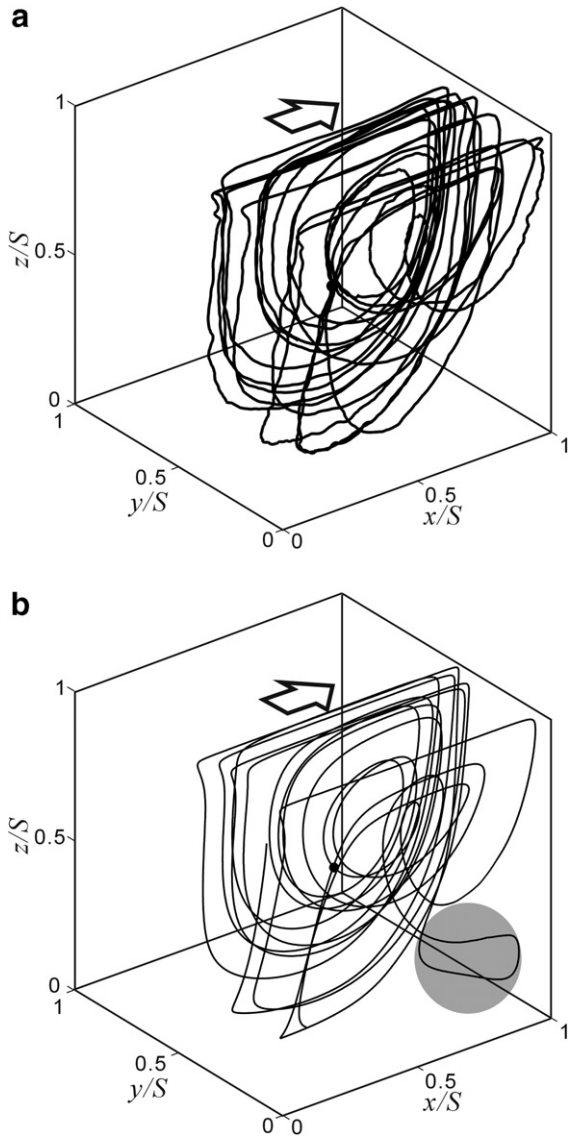

Fig. 11. Comparison of observed macro-particle trajectory segment (panel a) and calculated passive tracer trajectory (panel b) integrated from the same starting point (heavy dot on each panel). The excursion of the passive tracer into the corner eddy region is highlighted in gray.

be explained by steric effects. These are the geometric constraints that prevent solid macro-particles from getting too close to the rigid surfaces bounding the flow (top conveyor belt and cavity walls). If fluid pathways connecting different flow regions feature narrow passages close to rigid boundaries, then macro-particles may simply be too large to get through. In fact, the passive tracers and micro-particles found in Figs. 6 and 11b to transit from primary to secondary eddies do indeed pass through such narrow passages, located near intercept $y/S = 0.4$. Computed streamlines in this longitudinal plane are illustrated in Fig. 12.

As highlighted in Fig. 12, the streamline corridor leading fluid particles into the downstream corner eddy features two narrow throats near the upper downstream corner of the cavity. One is located along the moving lid, and the other lies near the top of the downstream end wall. The positions of the narrowest sections of the corridor and their corresponding widths b_1 and b_2 can be extracted from the computed flow field. This is illustrated in Fig. 12 for a longitudinal slice at intercept $y/S = 0.4$. The results for various transverse positions y/S

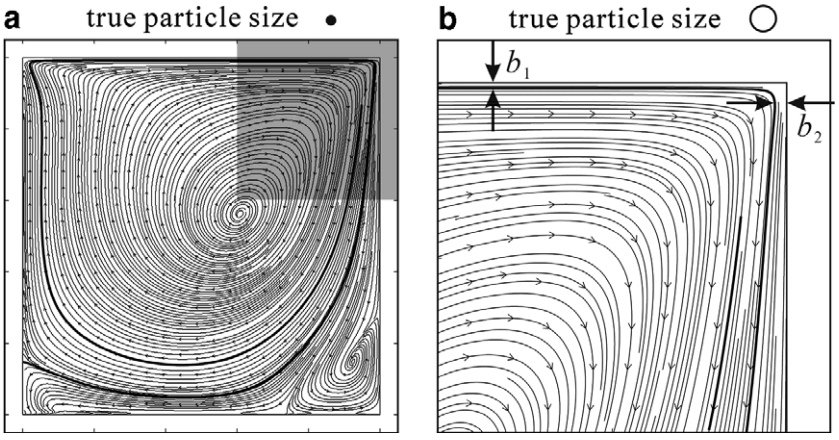

Fig. 12. Narrow throats located along the streamline corridor leading to the downstream corner eddy: (a) overall view; (b) close-up of the upper downstream corner of the cavity. The slice shown is located at transverse position $y/S = 0.4$.

Table 1
Positions and widths of the narrowest cross-sections along the streamline corridor leading to the downstream corner eddy (see Fig. 12 for a definition sketch)

Position of slice y/S	x/S	b_1 (mm)	z/S	b_2 (mm)
0.225	0.637	0.1	0.990	0.2
0.250	0.656	0.3	0.977	0.7
0.275	0.669	0.4	0.977	1.1
0.300	0.678	0.5	0.974	1.4
0.325	0.681	0.6	0.974	1.5
0.350	0.678	0.6	0.971	1.5
0.375	0.681	0.6	0.973	1.4
0.400	0.679	0.5	0.973	1.4
0.425	0.674	0.5	0.975	1.2
0.450	0.667	0.4	0.978	1.1
0.475	0.670	0.4	0.976	1.1
0.500	0.664	0.4	0.974	1.1

are listed in Table 1. For this Reynolds number ($Re = 470$), the widest available passage is found at intercept $y/S = 0.35$. Yet the throat widths in this plane are only $b_1 = 0.6$ mm along the top lid, and $b_2 = 1.5$ mm along the end wall. These are clearly small relative to the diameter of the macro-particle $d_M = 3$ mm, making it difficult for the particle to get through. Thus steric effects appear sufficient to explain the inability of a macro-particle to enter the downstream corner eddy. However other effects, associated with density and inertia, may also influence the global motions of the macro-particles, and are examined in the next section.

5. Density and inertia effects

In the previous section, observed macro-particle motions were compared with the simulated paths of passive tracers. Another way to probe the behaviour of macroscopic particles is to examine empirically their responses to changes in experimental conditions. Two such changes are examined in this section. A first sub-section looks at the effects of changing the density of the liquid relative to the particles. In a second sub-section, macroscopic particle trajectories are examined for different values of the cavity Reynolds number, varied in the range $Re = 130$ to 3200. The possible role of particle rotations is examined in a third sub-section.

5.1. Influence of relative density

Up to this point, macro-particle observations were presented only for the case of slightly buoyant particles (relative density mismatch $(\rho_f - \rho_M)/\rho_f \approx 0.05\%$). For that case, experiments are started with the spherical bead touching the top lid of the cavity. The driven lid motion then entrains the slightly buoyant particle along with the viscous fluid. The resulting spiraling paths of the macro-particles were found earlier to follow rather closely the corresponding fluid streamlines. For slightly buoyant macro-particles, any gravity-induced deviation would be expected to take the form of a slight upwards drift, but this drift can be kept in check by steric constraints every time the particle touches the moving upper lid, before being sent off again along spiraling orbits. The slightly buoyant particle trajectory depicted in Fig. 13 is seen to conform to these expectations.

To gain further insights into the macro-particle behaviour, it is useful to compare this case with the opposite situation, in which the macroscopic rigid sphere is slightly denser than the viscous liquid (negative relative density mismatch $(\rho_f - \rho_M)/\rho_f \approx -0.07\%$). In that case, the particle slowly sinks downwards in the quiescent liquid, and the experiment starts when the macro-particle has almost reached the rigid bottom of the cavity. The ensuing trajectory of the negatively buoyant particle is illustrated in Fig. 14. To allow comparison, the two experiments shown in Figs. 13 and 14 were conducted at lid speeds yielding the same value $Re = 470$ for the cavity Reynolds number.

For the negatively buoyant macro-particle tracked in Fig. 14, gravity-induced deviations are expected to take the form of a slow downwards drift, possibly allowing the particle to settle out of suspension when reaching the region of slow fluid velocity located along the cavity bottom. This does not occur, however, and the macro-particle is shown instead in Fig. 14 to be entrained by the fluid into spiraling motions that are very similar in character to those of the slightly buoyant particle shown in Fig. 13. The only difference is a slight distortion of the orbits, most notable upstream near the cavity sidewall. Elsewhere in the cavity, however, the particle paths are mostly unaffected by the switch from slightly positive to slightly negative buoyancy.

Once entrained into orbit, the slightly dense particle never falls out of suspension, as long as the steady lid motion continues to drive the flow. This indicates the existence of forces exerted by the viscous fluid on the denser solid particle, opposing its downwards gravitational drift and pulling the macro-particles towards the spiraling trajectories of the fluid flow. The magnitude of these forces can be roughly gauged from observation. In exploratory experiments, it was found that fluid motions at $Re = 470$ were unable to lift the slightly dense particle if the latter starts from rest, touching the rigid bottom. Fluid forces are thus relatively weak, strong enough to keep a slightly dense particle in suspension, but not enough to lift it up from the bottom.

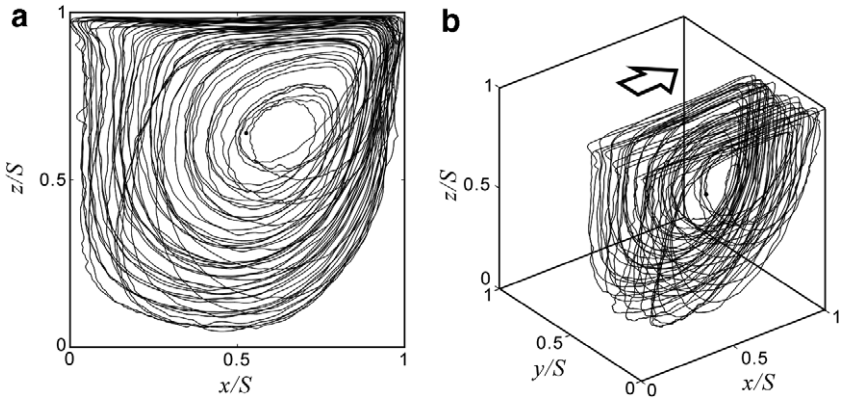

Fig. 13. Measured three-dimensional trajectory of a slightly buoyant macro-particle at $Re = 470$: (a) side view; (b) oblique view. The position history for this trajectory was depicted earlier in Fig. 8.

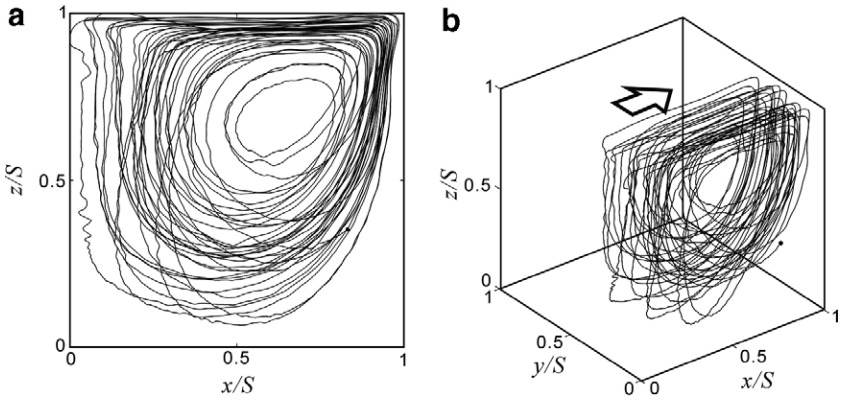

Fig. 14. Measured three-dimensional trajectory of a macro-particle slightly denser than the liquid, at $Re = 470$: (a) side view; (b) oblique view.

5.2. Influence of the Reynolds number

Like relative density, the respective roles of inertia and viscosity in determining macro-particle behaviour can be examined empirically by varying experimental conditions. For this purpose, a slightly buoyant particle in a liquid of constant composition is considered, and the cavity Reynolds number $Re = US/\nu$ is varied by driving the flow at different belt speeds. For Reynolds numbers $Re = 130$, 470 and 860, the kinematic viscosity $\nu = 37.2\ \mathrm{mm^2/s}$ and the density mismatch $(\rho_f - \rho_M)/\rho_f \approx 0.05\%$ are the same as before. For experiments at $Re = 3200$, a liquid composition of lower viscosity $\nu = 6.4\ \mathrm{mm^2/s}$ was prepared, and the corresponding density mismatch is $(\rho_f - \rho_M)/\rho_f \approx 0.10\%$. Using relation (2), the corresponding Stokes numbers take values $St = 0.006$, 0.023, 0.043 and 0.161. Like previously, each experiment starts from rest, with a single spherical bead present in the cavity, touching the top lid. The lid is set in motion at the desired speed, and the ensuing motion of the macro-particle is tracked by stereoscopic imaging.

Measured trajectories obtained in this fashion are presented in Fig. 15b–e, corresponding to Reynolds number values $Re = 130$, 470, 860 and 3200, respectively. To provide a point of reference, Fig. 15a shows the calculated path of a passive tracer in a cubic cavity driven at vanishingly small lid speed, corresponding to the Stokes flow limit $Re \to 0$. For Stokes flow, the equations governing the fluid and particle motions are invariant under time reversal. Combined with the fore/aft symmetry of our lid-driven cavity, this implies that a particle starting from a given point in the central transverse plane of the cavity will return to this same point. In accordance with this expectation, the calculated passive tracer trajectory shown in Fig. 15a forms a closed loop. The path of a neutrally buoyant rigid macroscopic sphere starting from the same point would be expected to deviate somewhat from this passive tracer trajectory, but it would be subject to the same symmetry constraint and would likewise be expected to trace a closed orbit.

In practice, experiments can only be conducted at finite values of the Reynolds number. Measured results for the relatively low value $Re = 130$ ($St = 0.006$) are shown in Fig. 15b. The observed macro-particle trajectory is similar in shape to the calculated Stokes flow orbit shown in Fig. 15a, but the orbit no longer closes on itself, featuring instead a tightly wound spiral. At the moderate Reynolds numbers $Re = 470$ and 860 ($St = 0.023$ and 0.043) depicted in Figs. 15c and d, the fore/aft symmetry of the flow is gradually lost due to the increasing influence of the convective accelerations. Also, the spiraling trajectories of the macro-particles unwind more rapidly, reflecting the increasing strength of the three-dimensional circulation inside the cavity. Note that for these Reynolds numbers, the liquid flow field inside the cavity remains steady in character, provided that start-up transients have dissipated and that time-dependent distortions due to the presence of macro-particles are neglected.

At the higher cavity Reynolds number $Re = 3200$ ($St = 0.161$), shown in Fig. 15(e), the observed macro-particle trajectory exhibits a qualitatively new feature. No longer is the particle confined to a single side of the cavity. Instead, the particle can pass from one side to the other, and back again given sufficient time, in

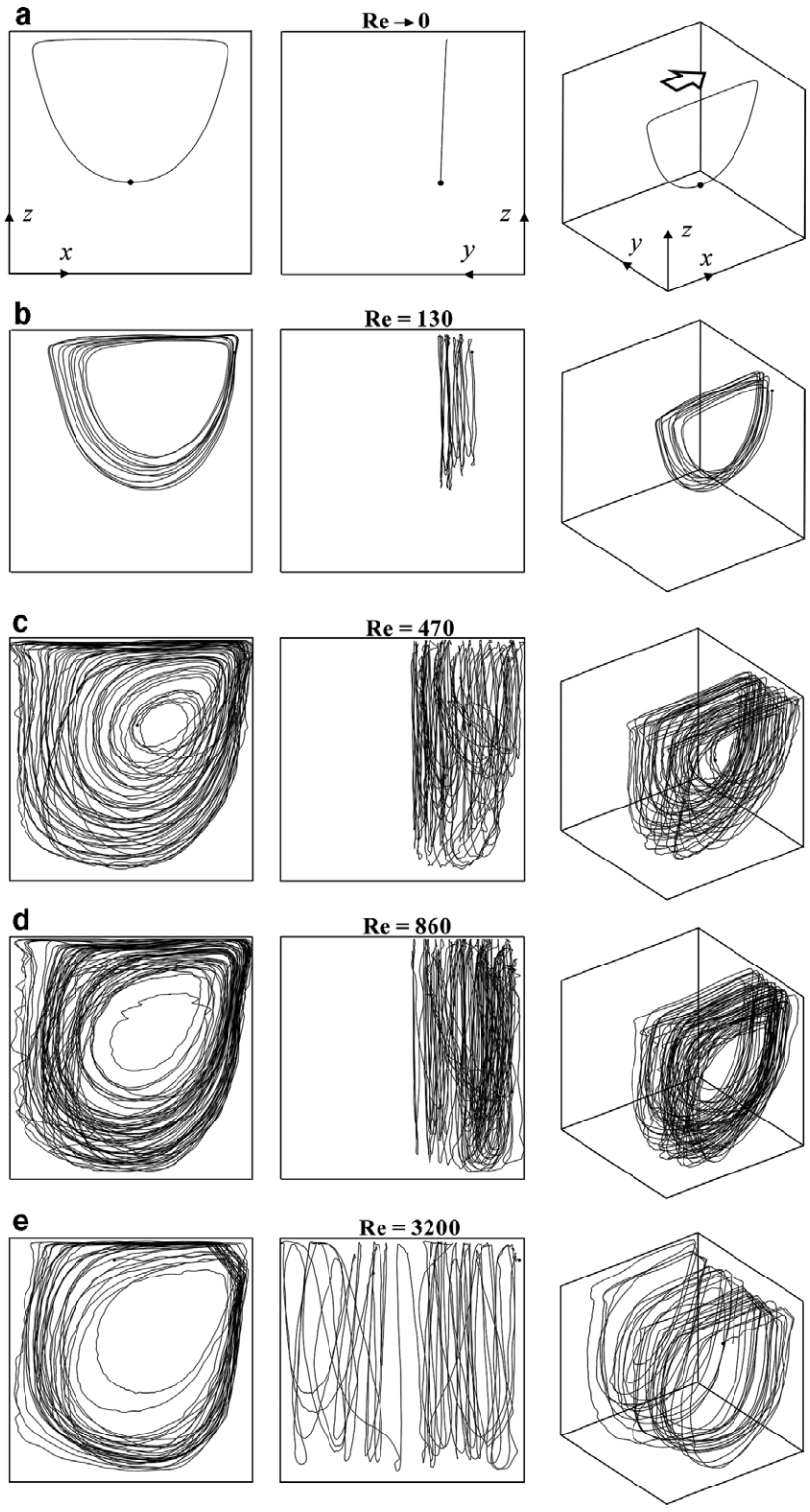

Fig. 15. Three-dimensional particle trajectories at different Reynolds numbers: (a) calculated passive tracer path in the Stokes flow limit $Re \to 0$; (b–e) measured macro-particle paths at Reynolds numbers $Re = 130$, 470, 860 and 3200 ($St = 0.006$, 0.023, 0.043 and 0.161), respectively. The left, middle and right panels show side, front and oblique views of the trajectories.

apparent violation of mirror symmetry. As shown by front view of the middle panel of 15(e), the corresponding spiraling path explores the full width of the cavity. Different explanations can be proposed for this newfound freedom of a particle to pass from one side of the cavity to the other. First, the Stokes number value ($St = 0.161$) is no longer so small, suggesting that a particle may more easily deviate from the fluid streamlines, hence cross the centre plane even if the fluid flow remains symmetric. A second explanation involves possible departures of the flow from steady state. Although the cavity is steadily driven by a belt operated at constant speed, it is possible that the liquid flow no longer settles down to a steady state at this higher Reynolds number. The time-dependent behaviour of the flow in a cubic cavity driven at $Re = 3200$ was earlier documented experimentally by Prasad and Koseff (1989) and numerically by Perng and Street (1989), and attributed to meandering Taylor–Görtler-like vortices. Perng and Street (1989) however, report that their numerical experiments showed no asymmetric perturbations. Other possible explanations ascribe the side-to-side particle motions to imperfections in the physical set-up, or to distortions of the local flow field by the macro-particle itself.

Presented on the left panels of Fig. 15, side views of the trajectories offer another perspective. A significant evolution is observed in the radial distribution of the macro-particle orbits with respect to the axis of rotation of the primary eddy. As the Reynolds number increases from $Re = 470$ to 3200 (with a corresponding increase of the Stokes number from $St = 0.023$ to 0.161), macro-particle orbits cluster within an increasingly narrow annulus. This annulus roughly coincides with a band of high liquid shear rate, nested between the nearly rigidly rotating core of the primary eddy, and the slowly counter-rotating corner eddies. As the Reynolds number increases, this shear band narrows and moves towards the periphery of the cavity. As observed in Fig. 15c–e, macro-particles are drawn towards this band, increasingly so at larger Reynolds numbers. We attribute this migration of macro-particle trajectories towards preferential orbits to the pull of fluid forces, originating from interactions between inertia and viscosity, and similar in origin to those found earlier to keep slightly dense particles in suspension.

To summarize, two competing trends are observed as the Reynolds number increases. Spanwise, macro-particles swerve laterally along spiraling orbits that unwind more and more loosely. Radially, on the other hand, the macro-particles migrate towards an orbital annulus that becomes more and more narrow. We interpret the spanwise trend as reflecting mostly changes in the liquid circulation pattern, while the radial pattern reflects the changing distribution of liquid shear rate and the action of fluid forces guiding the particles towards preferential orbits. The tendency of macro-particles to migrate towards the periphery, closer to the rigid boundary, as the Reynolds number increases, is observed as well in Poiseuille flow (Segré and Silberberg, 1962; Asmolov, 1999; Eloot et al., 2004). In the cavity flow case, however, observations are more difficult to interpret because changing the Reynolds number affects the structure of the liquid flow field in addition to controlling the interactions between macro-particles and the viscous liquid.

5.3. Particle rotations

Studies of macro-particle behaviour in Poiseuille flow have shown that the forces pulling particles towards equilibrium radial positions are associated with solid particle rotations relative to the suspending liquid (Kurose and Komori, 1999; Joseph and Ocando, 2002; Feng and Michaelides, 2003; Yang et al., 2005). Particle rotations could thus be expected to play a similar role in driving the observed convergence of macro-particles towards preferential orbits in our cavity flow experiments. This expectation can again be tested empirically. Although in the present work, we did not acquire complete time histories of three-dimensional particle rotations, partial measurements were obtained by filming a marked macro-particle along short trajectory segments. The case of a slightly buoyant particle in a cavity flow driven at Reynolds number $Re = 470$ is considered. As illustrated in Fig. 16a, an equatorial line was marked on the macro-particle allowing its rotation rate Ω_M (in plane x–z) to be measured from video images.

To estimate rotation rate relative to the fluid (in the absence of a macro-particle), information from the Navier–Stokes computations must be used. Assuming that the particle stays approximately in the same longitudinal plane (near transverse position $y/S = 0.4$), its 2D position (x, z) can also be retrieved. This makes it possible to estimate the local fluid rotation rate $\Omega_f = \frac{1}{2}\eta$, where η is the y-component of the vorticity vector obtained from the Navier–Stokes computations presented earlier.

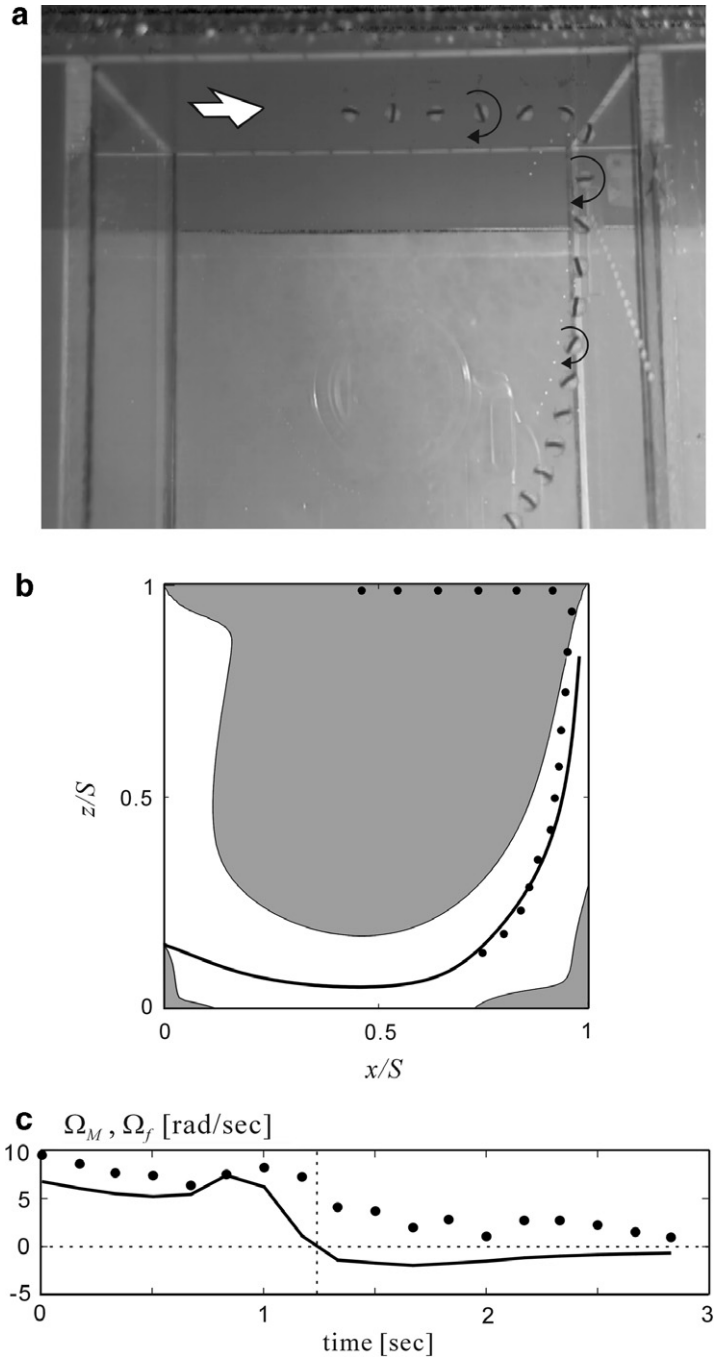

Fig. 16. Rotation of a marked macro-particle in the approximate plane $y/S \approx 0.4$ near the upper downstream corner of the cavity: (a) multiple-exposure video image; (b) particle path (dots) compared with the demarcation streamline (black line) and regions of positive (gray) and negative vorticity (white) in the plane $y/S = 0.4$; (c) comparison of the observed particle rotation rate (dots) with the local computed angular velocity of the fluid (line).

In Fig. 16b, the trajectory of the marked particle is presented on a background map displaying regions of positive (clockwise) and negative (counter-clockwise) fluid vorticity, shown in gray and white, respectively. Also represented is the demarcation streamline bounding the primary eddy, and we note in passing that the

reattachment point along the lower upstream end wall coincides with a zero contour of vorticity component η. The time evolution of the particle and fluid rotation rates experienced along the trajectory of the macro-particle is displayed in Fig. 16c.

Whereas earlier we found no significant local deviations between the macro-particle tracks and the fluid streamlines (see Fig. 7), Fig. 16 shows that the solid and fluid rotation rates do differ substantially. As the particle is entrained from left to right along the moving lid, it is rapidly spinned clockwise, just like fluid parcels would be in the absence of any solid particle. Near the downstream corner, however, the particle suddenly crosses into the region of counter-clockwise fluid vorticity. There the particle does not undergo the same spin reversal as the fluid parcels. Instead, it continues to rotate clockwise, albeit at a reduced rate, as it descends along the downstream end wall. Thus there is at least one segment of the macro-particle orbit along which its rotation rate is significantly different from the local fluid rotation rate. The macro-particle spinning rate is therefore significantly affected by angular inertia, and the resulting relative rotation can in turn be expected to play a dynamic role.

Taken together with our previous observations, these results suggest the following interpretation. As in Poiseuille flow, suspended macro-particles rotate relative to the fluid. Combined with distortions of the fluid shear rate caused by the rigid particle, these rotations induce weak but non-negligible normal-to-streamline forces between the fluid and particle. There are, however, special trajectories of the flow along which such forces balance out, and the macro-particles are pulled towards these preferential orbits.

Although this qualitative interpretation accounts for the empirical observations gathered in the present experiments, much further work will be required to put it on a quantitative footing. Mechanisms are difficult to describe quantitatively because, even for the simpler case of Poiseuille flow, the dynamic interaction between fluid and macro-particle involves a complicated combination of factors. Factors known to intervene include the presence of solid walls, and the local shear rate gradient experienced across the size of the particle, in addition to the density and rotation rate of the particle relative to the fluid (Feng et al., 1994; Matas et al., 2004b). As a result, past attempts to express the forces exerted on the particle and the induced relative motion using simple theoretical relationships or empirical correlations have not been successful. Even for the case of radially symmetric Poiseuille flow, fully coupled solutions of the Navier–Stokes equations with embedded solid particles appear necessary to capture the experimentally observed behaviour (Pan and Glowinski, 2005; Yang et al., 2005).

In two dimensions, computations of freely moving rigid disks in a square cavity have been carried out by Hwang et al. (2005). For the present case of three-dimensional cavity flow, however, no such solid–liquid computations have yet been attempted. In our pure fluid computations, the mesh resolution $\Delta x = \Delta y = \Delta z = 1.25$ mm is not sufficient to adequately resolve the solid macro-particles, much less to accurately describe the forces exerted along the solid–liquid boundary of the particle and its effect on the surrounding flow field. At present, it is therefore an open question whether fully coupled computations including inertia effects could reproduce the experimental observations described above.

6. Summary and conclusions

In the present paper, experiments and computations were used to probe the behaviour of macroscopic rigid spheres in lid-driven cavity flow. Care was first taken to characterize the flow field in the absence of macro-particles, using Navier–Stokes computations validated against observations of laser-illuminated micro-particles. At $Re = 470$, each side of the mirror-symmetric cavity features interconnected primary and corner eddies, between which physical micro-particles as well as simulated passive tracers can circulate. Spanwise secondary motions associated with the primary eddy are directed towards the sidewalls along the cavity periphery, and towards the centre plane in the core region. Aside from occasional excursions to the downstream corner eddy and back, passive tracers contained in the primary eddy follow spiraling paths, with rapid loops in the x–z plane modulated by irregular cycles of spanwise wandering.

This documented flow field was then used as reference to examine the motions of nearly neutrally buoyant macroscopic spheres suspended in the flow. Using stereoscopic imaging, three-dimensional position time his-

tories and trajectories were assembled for isolated macro-particles. The observed macro-particle motions were found to conform for the most part to the kinematic template provided by the fluid flow field. Irregularly cycling position histories associated with spiraling paths in the primary eddy region are highly similar in character to the corresponding paths of simulated passive tracers. Locally, macro-particle tracks also align closely with calculated fluid streamlines. In contrast with observed micro-particles and simulated passive tracers, however, macro-particles are not observed to transit from primary to corner eddy regions. This was tentatively attributed to steric effects hindering passage of solid particles of finite size through narrow throats in the fluid flow field.

The behaviour of macro-particles was then probed further by examining their responses to variations in experimental conditions. Macro-particle trajectories were found to be affected little by a switch from slightly positive to slightly negative buoyancy, demonstrating the existence of weak forces sufficient to compensate gravitational pull and keep in suspension particles slightly denser than the liquid. Experiments conducted at different lid speeds were also conducted to examine the influences of viscosity and inertia at different Reynolds numbers.

As the Reynolds number increases from $Re = 130$ to 3200, macro-particle paths exhibit competing trends. Spanwise, spiraling trajectories unwind more and more rapidly, exploring broader lateral swaths of the flow, including at $Re = 3200$ a newfound ability to pass from one side of the cavity to the other. Radially, on the other hand, macro-particles cluster more and more tightly within a preferential orbital annulus. Coinciding roughly with a band of rapid liquid shear rates, this annulus migrates towards the periphery of the cavity as the Reynolds number increases.

Convergence towards preferential orbits was interpreted to result from normal-to-streamline forces between the liquid and the macro-particles, pulling the macro-particles towards trajectories where these forces balance out, a process similar to the Segré–Silberberg effect of Poiseuille flow. Support for this interpretation is provided by indirect evidence, including the ability of the flow to suspend negatively buoyant particles and the dependence of the orbital clustering on the Reynolds number, as well as direct observations of particle rotations relative to the local fluid flow. A limitation of the present experiments, however, is that only a single particle diameter was examined. To check and refine the above picture, further experiments with particles of different diameters would be highly desirable.

Taken together, these findings have various implications for the relationship between macro-particle motions and the corresponding motions of passive tracers in the same viscous flow field. One implication is that the tracks of nearly neutrally buoyant macro-particles can be expected to align closely with the local paths of passive tracers. Alignment occurs despite the possible action of normal-to-streamline forces between fluid and particles, because macro-particles tend to migrate towards preferential trajectories where these forces balance out. The good news for flow visualization efforts based on the tracking of finite size particles is that the resulting particle motions faithfully represent the local fluid motions.

The flip side is that this local alignment by no means guarantees that macro-particle trajectories compose a faithful global picture of the flow. Two issues arise. First, steric effects may hinder passage of solid particles through narrow throats in the flow field, and possibly induce misleading conclusions regarding the topological connectivity of the flow. For the lid-driven cavity flows examined in the present work, for instance, macro-particles remain confined to the primary eddy despite the demonstrated existence of pathways linking the primary and corner eddies. Secondly, the convergence of macro-particles towards preferential trajectories prevents particles from distributing evenly within the flow field. Flow statistics based on macro-particle motions will therefore be biased towards particle-rich regions. Conversely, there will be particle-free regions (e.g. in our case the corner eddy and the inner core of the primary eddy) where no observations can be made.

This does not mean that no valuable global information on the flow can be gathered from macro-particle observations, but suggests that their interpretation should be taken with caution. Particle path observations should be complemented by information from other measurement approaches, or by direct numerical simulations. Likewise, from the point of view of prediction, small rigid bodies suspended in viscous fluids cannot be assumed to follow passive tracer paths everywhere. They may instead avoid certain regions or migrate towards preferential trajectories. This may have significant consequences for solid clots navigating the blood stream, and for other rigid bodies suspended in viscous flow fields.

Acknowledgements

Financial support for this work was provided by the National Science Council, Taiwan, and by the National Taiwan University through its Program for Excellence. We thank Professor T.P. Chiang (National Taiwan University) for useful discussions, Dr. D. Douxchamps (Nara Institute of Science and Technology, Japan) for help with his Coriander image acquisition software, and Dr. C.L. Chiu (National Taiwan University) for assistance in examining cavity flows in the Stokes flow limit.

References

Aref, H., 1990. Chaotic advection of fluid particles. Philos. Trans. Roy. Soc. London 333, 273–288.
Asmolov, E.S., 1999. The inertial lift on a spherical particle in a plane Poiseuille flow at large channel Reynolds number. J. Fluid Mech. 381, 63–87.
Batchelor, G.K., 1967. An Introduction to Fluid Dynamics. Cambridge University Press.
Bretherton, F.P., 1962. The motion of rigid particles in a shear flow at low Reynolds number. J. Fluid Mech. 14, 284–304.
Burggraf, O.R., 1966. Analytical and numerical studies of the structure of steady separated flows. J. Fluid Mech. 24, 113–151.
Capart, H., Young, D.L., Zech, Y., 2002. Voronoï imaging methods for the measurement of granular flows. Exp. Fluids 32, 121–135.
Chen, Y.C., Stårner, S.H., Masri, A.R., 2006. A detailed experimental investigation of well-defined, turbulent evaporating spray jets of acetone. Int. J. Multiphase Flow 32, 389–412.
Chiang, T.P., Sheu, W.H., 1997. Numerical prediction of eddy structure in a shear-driven cavity. Comput. Mech. Eng. 20, 379–396.
Chiang, T.P., Hwang, R.R., Sheu, W.H., 1997. On end-wall corner vortices in a lid-driven cavity. J. Fluids Eng. 119, 201–204.
Chiang, T.P., Sheu, W.H., Hwang, R.R., 1998. Effect of Reynolds number on the eddy structure in a lid-driven cavity. Int. J. Numer. Methods Fluids 26, 557–579.
Chien, W.L., Rising, H., Ottino, J.M., 1986. Laminar mixing and chaotic mixing in several cavity flows. J. Fluid Mech. 170, 355–377.
Eloot, S., De Bisschop, F., Verdonck, P., 2004. Experimental evaluation of the migration of spherical particles in three-dimensional Poiseuille flow. Phys. Fluids 16, 2282–2293.
Feng, J., Hu, H.H., Joseph, D.D., 1994. Direct simulation of initial values problems for the motion of solid bodies in a Newtonian fluid. Part 2. Couette and Poiseuille flows. J. Fluid Mech. 277, 271–301.
Feng, Z.G., Michaelides, E.E., 2003. Equilibrium position for a particle in a horizontal shear flow. Int. J. Multiphase Flow 29, 943–957.
Freitas, C.J., Street, R.L., Findikakis, A.N., Koseff, J.R., 1985. Numerical simulation of three-dimensional flow in a cavity. Int. J. Numer. Methods Fluids 5, 561–575.
Gary, J., McCormick, S., Sweet, R., 1983. Successive overrelaxation, multigrid, and preconditioned conjugate gradients algorithms for solving a diffusion problem on a vector computer. Appl. Math. Comput. 13, 285–309.
Guermond, J.L., Migeon, C., Pineau, G., Quartapelle, L., 2002. Start-up flows in a three-dimensional rectangular driven cavity of aspect ratio 1:1:2 at $Re = 1000$. J. Fluid Mech. 450, 169–199.
Han, M., Kim, C., Kim, M., Lee, S., 1999. Particle migration in tube flow of suspensions. J. Rheol. 43, 1157–1174.
Ho, B.P., Leal, L.G., 1974. Inertial migration of rigid spheres in two-dimensional unidirectional flows. J. Fluid Mech. 65, 365–400.
Hu, H.H., 2001. Direct simulation of flows of solid–liquid mixtures. Int. J. Multiphase Flow 22, 335–352.
Hu, H.H., Patankar, N.A., Zhu, M.Y., 2001. Direct numerical simulations of fluid–solid systems using the arbitrary Lagrangian–Eulerian technique. J. Comput. Phys. 169, 427–462.
Hwang, W.R., Anderson, P.D., Hulsen, M.A., 2005. Chaotic advection in a cavity flow with rigid particles. Phys. Fluids 17, 1–12.
Hwu, T.Y., 2006. Fluid stirrings in a circular cavity with various driven boundaries. Eur. J. Mech. B, Fluids 25, 192–203.
Inamuro, T., Maeba, K., Ogino, F., 2000. Flow between parallel walls containing the lines of neutrally circular cylinders. Int. J. Multiphase Flow 26, 1981–2004.
Joseph, D.D., Ocando, D., 2002. Slip velocity and lift. J. Fluid Mech. 454, 263–286.
Kalman, R.E., 1960. A new approach to linear filtering and prediction problems. J. Basic Eng. D 82, 35–45.
Koseff, J.R., Street, R.L., 1984a. Visualization studies of a shear driven three-dimensional recirculating flow. J. Fluids Eng. 106, 21–27.
Koseff, J.R., Street, R.L., 1984b. On end wall effects in a lid-driven cavity flow. J. Fluids Eng. 106, 385–389.
Koseff, J.R., Street, R.L., 1984c. The lid-driven cavity flow: a synthesis of qualitative and quantitative observations. J. Fluids Eng. 106, 390–398.
Kurose, R., Komori, S., 1999. Drag and lift forces on a rotating sphere in a linear shear flow. J. Fluid Mech. 384, 183–206.
Lo, D.C., Murugesan, K., Young, D.L., 2005. Numerical solution of three-dimensional velocity–vorticity Navier–Stokes equations by finite difference method. Int. J. Numer. Methods Fluids 47, 1469–1487.
Matas, J.-P., Morris, J.F., Guazzelli, E., 2004a. Inertial migration of rigid spherical particles in Poiseuille flow. J. Fluid Mech. 515, 171–195.
Matas, J.-P., Morris, J.F., Guazzelli, E., 2004b. Lateral forces on a sphere. Oil Gas Sci. Technol. – Revue IFP 59, 59–70.
Migeon, C., 2002. Details on the start-up development of the Taylor–Gortler-like vortices inside a square-section lid-driven cavity for $1000 \leqslant Re \leqslant 3200$. Exp. Fluids 33, 594–602.
Migeon, C., Pineau, G., Texier, A., 2003. Three-dimensionality development inside standard parallelepipedic lid-driven cavities at $Re = 1000$. J. Fluids Struct. 17, 717–738.

Pan, F., Acrivos, A., 1967. Steady flows in rectangular cavities. J. Fluid Mech. 28, 643–655.
Pan, T.-W., Glowinski, R., 2005. Direct simulation of the motion of neutrally buoyant balls in a three-dimensional Poiseuille flow. C. R. Mec. 333, 884–895.
Perng, C.Y., Street, R.L., 1989. Three-dimensional unsteady flow simulations: alternative strategies for a volume-averaged calculation. Int. J. Numer. Methods Fluids 9, 341–362.
Pozrikidis, C., 1992. Boundary Integral and Singularity Methods for Linearized Viscous Flow. Cambridge University Press.
Prasad, A.K., Koseff, J.R., 1989. Reynolds number and end-wall effects on a lid-driven cavity flow. Phys. Fluids A 1, 208–218.
Prevost, F., Boree, J., Nuglisch, H.J., Charnay, G., 1996. Measurements of fluid/particle correlated motion in the far field of an axisymmetric jet. Int. J. Multiphase Flow 22, 685–701.
Ramanan, N., Homsy, G.M., 1994. Linear stability of lid-driven cavity flow. Phys. Fluids 6, 2690–2701.
Rhee, H.S., Koseff, J.R., Street, R.L., 1984. Flow visualization of a recirculating flow by rheoscopic liquid and liquid crystal techniques. Exp. Fluids 2, 57–64.
Rubinow, S.I., Keller, J.B., 1961. The transverse force on a spinning sphere moving in a viscous fluid. J. Fluid Mech. 11, 447–459.
Saffman, P.G., 1965. Lift on a small sphere in a slow shear flow. J. Fluid Mech. 22, 385–400.
Shankar, P.N., 1998. Three-dimensional Stokes flow in a cylindrical container. Phys. Fluids 10, 540–549.
Shankar, P.N., Deshpande, M.D., 2000. Fluid mechanics in the driven cavity. Ann. Rev. Fluid Mech. 32, 93–136.
Shu, C.-W., Osher, S., 1988. Efficient implementation of essentially non-oscillatory shock capturing schemes. J. Comput. Phys. 77, 439–471.
Shu, C., Wang, L., Chew, Y.T., 2003. Numerical computation of three-dimensional incompressible Navier–Stokes equations in primitive variable form by DQ method. Int. J. Numer. Methods Fluids 43, 345–368.
Segré, G., Silberberg, A., 1961. Radial particle displacements in Poiseuille flow of suspensions. Nature 189, 209–210.
Segré, G., Silberberg, A., 1962. Behaviour of macroscopic rigid spheres in Poiseuille flow. Part 2. Experimental results and interpretation. J. Fluid Mech. 14, 136–157.
Spinewine, B., Capart, H., Larcher, M., Zech, Y., 2003. Three-dimensional Voronoï imaging methods for the measurement of near-wall particulate flows. Exp. Fluids 34, 227–241.
Staben, M.E., Davis, R.H., 2005. Particle transport in Poiseuille flow in narrow channels. Int. J. Multiphase Flow 31, 529–547.
Swaminathan, T.N., Hu, H.H., Patel, A.A., 2006. Numerical analysis of the hemodynamics and embolus capture of a Greenfield vena cava filter. J. Biomech. Eng. 128, 360–370.
Tsorng, S.J., 2006. Three-dimensional particle paths in a lid-driven cavity flow: experiments and analysis. Ph.D. Thesis, National Taiwan University.
Tsorng, S.J., Capart, H., Lai, J.S., Young, D.L., 2006. Three-dimensional tracking of the long time trajectories of suspended particles in a lid-driven cavity flow. Exp. Fluids 40, 314–328.
Wu, X.H., Wu, J.Z., Wu, J.M., 1995. Effective vorticity–velocity formulations for three-dimensional incompressible viscous flows. J. Comput. Phys. 122, 68–82.
Yang, T.S., Shy, S.S., 2005. Two-way interaction between solid particles and homogeneous air turbulence: particle settling rate and turbulence modification measurements. J. Fluid Mech. 526, 171–216.
Yang, B.H., Wang, J., Joseph, D.D., Hu, H.H., Pan, T.-W., Glowinski, R., 2005. Migration of a sphere in tube flow. J. Fluid Mech. 540, 109–131.
Zang, Y., Street, R.L., Koseff, J.R., 1993. A dynamic mixed subgrid-scale model and its application to turbulent recirculating flows. Phys. Fluids. A 5, 3186–3196.